Journal of Materials Science: Materials in Electronics (2020) 31:8780–8795
https://doi.org/10.1007/s10854-020-03413-8

Rose cyanidin 3,5-di-*O*-glucoside-assisted gold nanoparticles, their antiradical and photocatalytic activities

Elham Shafik Aazam[1] · Zoya Zaheer[1]

Received: 13 January 2020 / Accepted: 13 April 2020 / Published online: 23 April 2020
© Springer Science+Business Media, LLC, part of Springer Nature 2020

Abstract
Cyanidin 3,5-di-*O*-glucoside anthocyanin was extracted from red rose flower petals and used as reducing and capping agent for the green synthesis of anisotropic gold nanoparticles (Au NPs). Transmission electron microscope (TEM) images indicated that the Au NPs have large number of small spheres of gold. Surface plasmon resonance band position strongly depended on the [$HAuCl_4$] and [anthocyanin]. Cationic surfactant distinctly changed the shape, size, number of NPs, and size distribution of Au nanodisks at room temperature. Conventional techniques were used to the estimate the antiradical and antimicrobial activities of the cyanidin 3,5-di-*O*-glucoside anthocyanin and gold NPs. The 2,2-diphenyl-L-picrylhydrazyl nitrogen radical ($DPPH^{\cdot}$), two bacteria strains (Staphylococcus aureus and Escherichia coli), and two yeast strains (Candida albicans ATCC 10231 and Candida parapsilosis ATCC 22019) were used to determine the antioxidant and antimicrobial properties of CTAB-capped gold NPs. Eosin yellow photocatalytic degradation followed apparent first-order kinetics with activation energies of 54.4 kJ/mol and 39.5 kJ/mol, respectively, for oxidative and sunlight catalyzed paths. The photocatalytic rates drastically inhibited with scavengers, demonstrating that the reactive radical oxygen species ($HO^{\cdot}$ and $O_2^{-\cdot}$), holes (h^+) and electrons (e^-) played major role in the degradation.

1 Introduction

Due to the potential application in biology, catalysis, medicine, and nonlinear optics, the fabrication of advanced transition metal NPs of gold by various methods such as chemical radiation, and seed growth has been reported on several occasions from many decades [1–5]. For example, Enustun and Turkevich used chemical reduction approach and reported the preparation of Au nanoparticles at room temperature [2]. Henglein et al. used irradiation technique to prepare advanced Au nanoparticles having 15 nm diameters [3]. These nanoparticles have also been synthesized with radiation reduction of $HAuCl_4$ solution by using cationic hexadecyltrimethylammonium chloride surfactant as a stabilizing and capping agent [4]. Goia and Matijevic were developed a simple chemical reduction for the synthesis of mono-dispersed gold sols by using sodium ascorbate at room temperature [5]. They also suggested that the particle size could be tuned by altering the pH of the reaction solution. Bakshi and his coworkers used various stabilizers (surfactants, polymers, proteins, phospholipids, and enzymes) to control the morphology gold NPs and suggested that the CTAB surfactant was the best capping agent [6–8]. It has been established that the presence of a suitable stabilizer and/or capping agent such as surfactant, enzyme, ligand, metalloporphyrin, carbohydrate, protein, and solvent are mandatory to the synthesis of small size particles [9–12]. Khan and his coworkers reported yellow colored precipitate between $HAuCl_4$ and CTAB with in the time of mixing. They also suggested that mixing order of $HAuCl_4$, ascorbic acid, and CTAB has significant impact on the morphology (size, shape, and size distribution) of resulting nanogold [13]. Paracetamol, pain reliever and fever reducer drug, was used to the preparation of gold NPs having different morphologies with shape-controlling cationic surfactant, cetyltrimethylammonium bromide [14]. Literature contains abundant reports to the preparation of gold nanomaterials that may pose a risk, which might be adsorption of organic solvents, polymers, ligands, zeolites, and surfactants [15–18]. Therefore, various researchers used plants, seeds, leaves, flowers, bacteria, yeast, etc. to the synthesis of monometallic and

✉ Zoya Zaheer
zoya.zaheer@gmail.com

[1] Department of Chemistry, Faculty of Science, King Abdulaziz University, P. O. Box 80203, Jeddah 21589, Saudi Arabia

bimetallic nanomaterials of gold [19, 20]. Shingaravelu et al. were used flower of couroptia guianesis flowers to the fabrication of gold NPs. They also demonstrated that couroupita guianesis-capped gold has potential anticancer activity [21].

Eugster and Marki-Fischer presented a survey of pigments present in the variety of rose flowers in his pioneering article. They pointed out that the many roses contain large amount of medicinally active constituents such as anthocyanins, cyanins, and carotenoids [22]. Eikani and his coworkers used simultaneous distillation–extraction method for the recovery of water-soluble constituents present in the extract of rose oil [23] and reported the presence of various odorous constituents. Nowak et al. reported the antimicrobial properties and chemical compositions of the rose petals [24]. The advanced nanomaterials would be prepared by using medicinally important plants and their parts. Their chemical constituents (alkaloids, terpenoids, polyphenols, starch and other biomolecules) have been acted as reducing agents with and without shape-directing cetyltrimethylammonium bromide [25–27]. Our goal in this study was to synthesize the gold nanoparticles by using cyanidin 3,5-di-*O*-glucoside (extracted from an aqueous extract of red rose flower) and $HAuCl_4$ with and without shape-controlling CTAB. We also focused on providing a more simple, cost-effective, and reproducible technique to the synthesis of pure gold NPs. Antiradical and antimicrobial activities of cyanidin 3,5-di-*O*-glucoside anthocyanin and as-prepared gold NPs were determined against human pathogens. The possible mechanism of $AuCl_4$ interaction with anthocyanin has been discussed. The as-synthesized AuNPs used as an electron relay transfer catalyst for the oxidative and photocatalytic degradation of eosin yellow (C. I. Acid red 87, red fluorescent active dye, photoinitiator to develop papanicolaou stain).

2 Experimental section

2.1 Chemicals

The gold(III) chloride trihydrate ($HAuCl_4 \cdot 3H_2O$ and purity ≥ 99.9%), eosin yellow ($C_{20}H_6Br_4Na_2O_5$, molar mass = 647.89 and purity 99%) ,cetyltrimethylammonium bromide ($C_{19}H_{42}NBr$, and molecular weight = 364.45 g/mol), and sodium salt of eosin yellow ($C_{20}H_6Br_4O_5Na_2$, red powder and molar mass = 647.89 g/mol) were purchased from Sigma-Aldrich, USA, and there stock solutions were prepared in deionized water by molarities basis. All chemicals such as gallic acid, 2,2-diphenyl-L-picrylhydrazyl radical, ethanol, dimethyl sulfoxide (DMSO), and Folin–Ciocalteu reagent were of analytical grade.

2.2 Instruments

The UV–Vis spectra of as-prepared gold NPs were recorded by using Shimadzu UV-260 spectrophotometer. The surface morphology of NPs was determined by using conventional scanning electron microscope (SEM), transmission electron microscope (TEM, JEM 2100), equipped with energy-dispersed X-ray detector (EDX). For TEM measurement, resulting sols were deposited on a carbon-coated copper grid, dried at room temperature under open air. The specific surface area of these NPs was estimated from nitrogen adsorption–desorption isotherms (Brunauer–Emmett–Teller; BET) by using Quantachrome Nova 3200e Surface area & pore size analyzer, Instrument. The morphology and elemental composition of anthocyanin capped AuNPs were determined using field emission electron microscope with QUANTA FEG 450, FEI Company, Eindhoven, The Netherland. UV–Vis diffuse reflectance spectra were recorded on an Agilent-Varian Carry 5000 spectrophotometer.

2.3 Determination of cyanidin 3,5-di-*O*-glucoside and phytochemicals

Red rose flowers petals were cleaned thoroughly with deionized CO_2-free water to remove the dust and other unwanted materials and shade dried at 30 °C temperatures for ca. 1 week. The petals were then ground well into powder by manual blender. The extract was prepared by mixing 2 g powder of petals with 250 ml of double distilled water in a 500-ml reaction vessel and was placed in magnetic stirrer hot plate at 80 °C for 3 h. The resulting red color solution was cooled, filtered, collected in an amber glass colored bottle, and stored in a refrigerator.

For the determination of total phenolic contents in as-prepared rose petal extract, Singleton and Rossi colorimetric method was used with slight modification [28]. The phosphomolybdic-phosphotungstic and gallic acid were used as a reagent and standard reference, respectively. In a typical experiment, 5.0 ml of extract is added in a volumetric flask containing 50 ml distilled water, 5 ml regent, and 10 ml 20% sodium carbonate solution. The reaction solution was mixed thoroughly and absorbance of the resulting blue color was measured at 670 nm after 1 h. The extraction of cyanidin anthocyanin was carried out in double distilled water and their concentration was estimated by using spectrophotometric method [29, 30]. The molar extinction coefficient (=30,247 L/mol cm) of cyanidin anthocyanin and absorbance ($A = [(A_{522} - A_{700})_{pH1.2} - (A_{525} - A_{700})_{pH4.3}]$ was used for the estimation of total anthocyanin contents. Optical image of red rose flower, structure of extracted cyanidin 3, 5-di-*O*-glucoside, and its optical image of red color are given in Scheme 1.

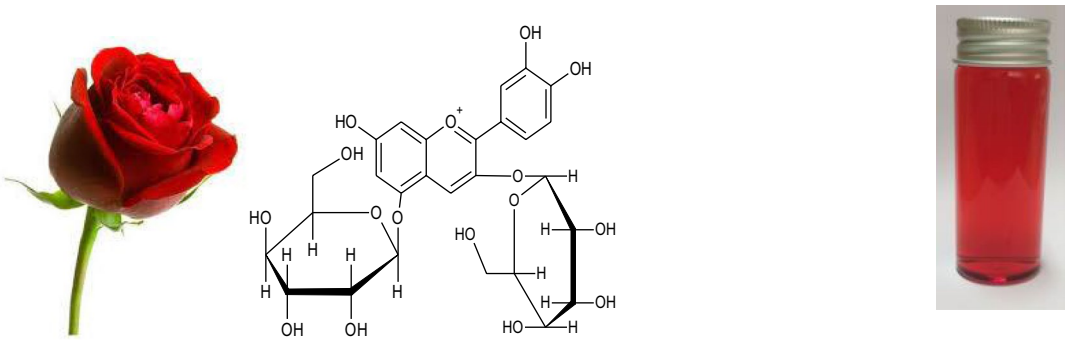

Scheme 1 Photograph of red rose flower, structure of cyanidin 3,5-di-*O*-glucoside, and image of extracted red color from rose petals

2.4 Preparation of gold nanoparticles

In order to optimize the process parameters, the factorial design of experiments (one factor at a time) method was used in this study. In a typical experiment, the different concentrations of gold solutions (25, 30, 40, 50, and 60×10^{-5} mol/dm^3) were added into the reaction flasks having cyanidin anthocyanin and diluted with deionized water accordingly (total volume = 50 ml of each experiment). The reaction was slow and pale yellow reaction mixture became reddish turbid after 1 h at room temperature. Interestingly, the purple color appeared within 20 min and the resulting color was stable for ca. 3 days (no further color change was observed), indicating the formation of gold NPs during the redox reaction between Au^{3+} ions and active constituent of rose extract. For the solid separation, the resulting gold sols were centrifuged at 15,000 rmp for 25 min. The resulted mass was washed with water to remove the unreacted reactants from the surface of gold NPs. To study the effect of petal extract concentration on the morphology of gold NPs, the extract concentration was varied from 10 to 40% at 30×10^{-5} mol/L Au^{3+} ions.

2.5 DPPH antiradical scavenging activity

The DPPH radical solution (0.001 mol/L^1) was prepared in methanol. The 2.0 cm^3 radical solution was mixed with 5.0 cm^3 of rose extract at 30 °C. The antioxidant efficiency was measured at 517 nm (λ_{max} of DPPH radical) as a function of time [31]. The ascorbic acid was used as a controls. The percentage of DPPH scavenging activity was determined by using Eq. (1). All measurements were taken in triplicate.

$$\%\ DPPH\ activity = \left[\frac{1 - (absorbance\ of\ sample - absorbance\ of\ blank)}{absorbance\ of\ control}\right] \times 100 \quad (1)$$

2.6 Antimicrobial activity

The micro-broth dilution method was used for the evaluation of antimicrobial properties of cyanidin 3,5-di-*O*-glucoside and gold NPs. The minimum inhibitory concentration (MIC) was estimated according to the reported method. For this purpose, two bacterial strains, namely *Staphylococcus aureus* ATCC 25923) and *Escherichia coli* ATCC 25922, were used. Gentamicin and dimethyl sulfoxide were used as a reference and negative control, respectively. For the antifungal activity of red rose extract and gold NPs, two reference yeast strains (*Candida albicans* ATCC 10231 and *Candida parapsilosis* ATCC 22019) were used. Mueller–Hinton agar was utilized for the dilution. Fluconazole was used as a reference compound. Each experiment was performed in triplicate.

2.7 Catalytic degradation of eosin yellow

To determine the catalytic efficiency, eosin yellow aqueous solution 2.0×10^{-5} mol/dm^3 was added into a reactor containing required $NaBH_4$ and equilibrated at room temperature for 30 min. Then aqueous suspension of AuNPs, nanocatalyst (3.4×10^{-4} mol/L) was added. The decomposition of dye was monitored by recording the spectra of reaction mixture as constant time intervals. For photocatalytic degradation, the same reaction mixture was exposed to sunlight irradiation for 20 min. The effect of scavengers (methanol, benzoquinone, potassium bromate, potassium iodide, and ammonium oxalate) was also studied to establish the role of holes, electrons, and reactive oxygen radicals on the rate of dye degradation.

3 Results and discussion

3.1 Interaction and morphology of CTAB-gold complex

Upon addition of an required RRF extract into the reaction vessel containing $HAuCl_4$, a yellowish-blue turbidity appeared after 10 min and the solution was not perfect. The formation of purple color was very slow and the resulting color was not perfect transparent. Xiao and Qi in his featured article pointed out that metal–surfactant complex-template is an excellent method for the controlled synthesis of nanocrystals [32]. Oi et al. prepared curled nanobelts having 50–100 nm thickness by using $HAuCl_4$ and cationic surfactant in solution without any reductant [33]. In order to see insight into this type of interactions between CTAB and gold salt, different [CTAB] (from 0.1 to 3.5 mM/L) were added in a solution containing fixed $[HAuCl_4] = 0.05$ mM/L. Visual observations indicate the appearance of golden yellow when CTAB was mixed with $HAuCl_4$ solution, which should be due to the formation of gold-CTAB complex between the positive $(-N^+(CH_3)_3)$ head group of ionized CTAB and negative $AuCl_4^-$ through electrostatic interactions. Inspection of Fig. 1 clearly demonstrated that the shape of the gold-CTA spectra depends on the reaction time at room temperature [34].

The TEM images further illustrate that aqueous CTA- $HAuCl_4$ complex has anisotropic morphology of nanoflower-like gold-CTA (Fig. 1), which makes them self-assembled and crystallized into a two-dimensional mono-disperse NPS. The observed morphology can be attributed to shape anisotropy. In Figure 1, TEM image also shows that there is a large fraction of gold salt solubilized into the aggregates of CTAB, which results in a large anisotropy. The following mechanism was proposed to the formation of $AuCl_4$–CTA complex [13] (Scheme 2).

Scheme 2 represents the complex formation between ionized CTAB, i.e., CTA ions and $AuCl_4^-$ ions.

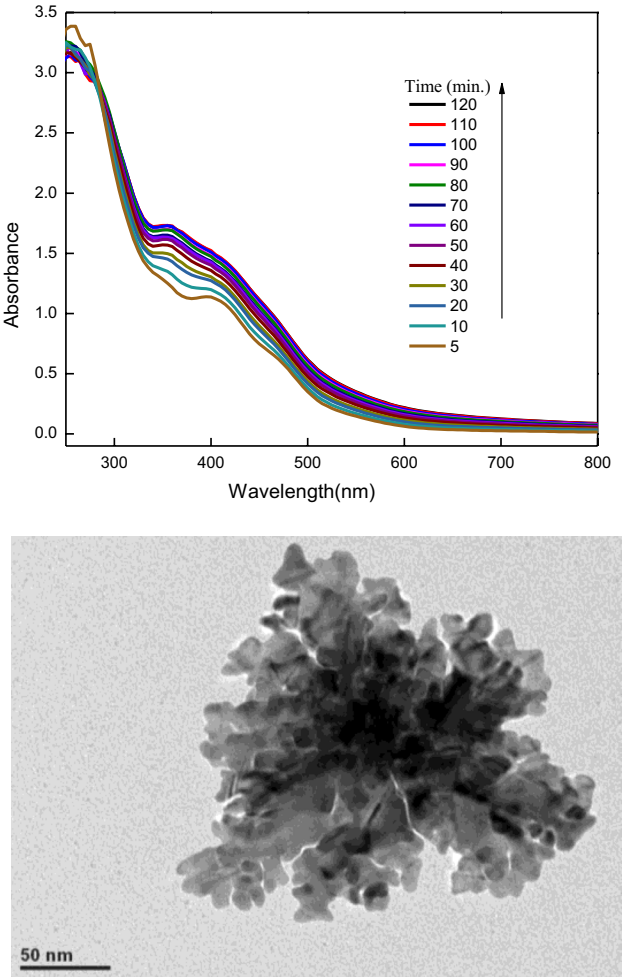

Fig. 1 UV–Vis spectra and TEM images of an aqueous solution of CTAB (10.0×10^{-4} mol/L) and $HAuCl_4$ (10.0×10^{-4} mol/L) as a function of time at room temperature

3.2 Morphology of gold NPs

In order to prepare gold NPs, the required amount of cyanin anthocyanin was added into the orange-yellow colored $AuCl_4$–CTA complex (vide supra). The red color reaction mixture became purple as the reaction time increases, indicating the reduction of gold-CTA complex by cyanin anthocyanin. TEM images of anthocyanin capped gold NPs are given in Fig. 2a. Inspection of these results clearly suggest that the resulting NPs have various morphology ranging from spheres, nanodisks and triangular nanoplate with broader size distribution (presence of triangular gold NPs as the main product as circled in the image). Figure 2b shows the TEM image of CTAB stabilized gold NPs. Comparison of these TEM images indicates that the number of NPs decreased in the presence of CTAB. Only few gold nanodisks (thickness = 15 to 25 nm) were formed instead of large number of nanospheres. $HAuCl_4$ and active anthocyanin are incorporated into the micelles of CTAB. The redox reaction takes place in the Stern layer of micelles. Finally, pale yellow Au^{3+} ions were reduced to gold metal (purple colored gold sols), which leads to the formation of triangular nanodisks of gold. These observations are in accordance with the hypothesis and results of Xiao and Qi and other investigators regarding the surfactant-assisted morphology of decahedral gold-nanodisks containing twinned crystals display five-twin boundaries, with all crystal faces formed by {111} planes [32, 35, 36].

For spherical NPs, surface area was estimated with Eq. (2).

Scheme 2 Complex formation between $AuCl_4$ and CTAB

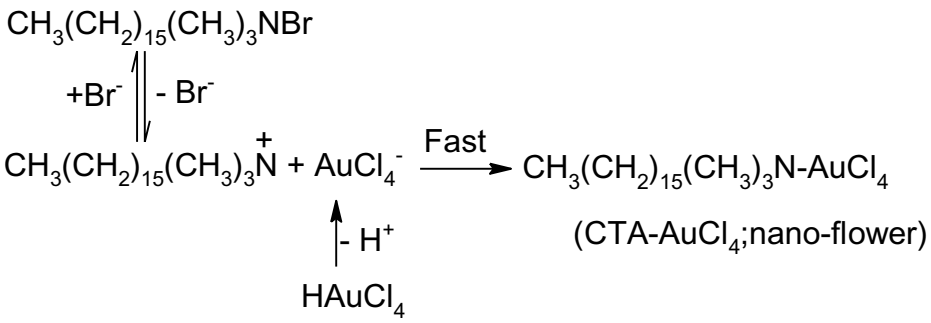

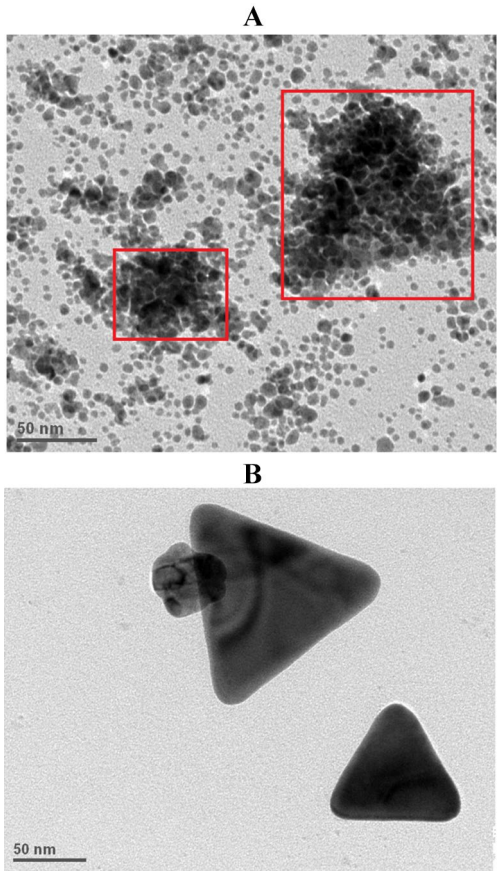

Fig. 2 TEM images of cyanidin-gold NPs (**a**) and CTAB-capped gold NPs (**b**)

$$SSA = \frac{surface\ area\ of\ gold\ NPs}{mass\ of\ gold} = \frac{6}{\pi\, d_{TEM}} \quad (2)$$

where ρ = density of pure gold (= 19,320 kg/m^3) and d_{TEM} = diameter of gold NPs. The theoretical SSA was found to be 98,904 m^2/kg for gold NPs with 20 nm diameter. The particle size (d_{BET}) was also calculated by using the experimental BET surface area of as-prepared gold NPs (99,500 m^2/kg) from Eq. (3).

$$d_{BET} = \frac{6}{\rho\, SSA} \quad (3)$$

where SSA is the specific surface area. The d_{BET} indicates that an average particle diameter ca. 31 nm. Sau and Murphy also reported the synthesis of a number of gold nanostructures in high yield under ambient conditions [36]. The presence of a thick black layer was also visualized on the surface of nanodisk, which indicates the capping action of anthocyanin [37, 38]. In order to determine the presence of elements in the anthocyanin-capped AuNPs, the field emission scanning electron microscope elemental mapping image was recorded. Figure 3 shows the presence of mainly metallic gold along with carbon and oxygen, which might be due to the presence of anthocyanin on the surface of resulting NPs.

3.3 Mechanism of gold NPs formation

It has been established that pH has a significant impact on the electron transfer from metal ions to the reducing agent in an aqueous solution [39]. Nucleation and growth depend on the pH of the reaction solution. On the other hand, red, violet, blue, and colorless species of cyanidin 3,5-di-*O*-glucoside anthocyanin also exist in solution due to the presence of delocalized conjugated system and –OH groups. The pH of the working reaction mixture containing different concentrations of $HAuCl_4$, CTAB and cyanidin was recorded (Table 1). It was observed that the variation of CTAB and cyanidin has no significant effect on the pH, which remains nearly constant. On the other hand, color of the cyanidin 3,5-di-*O*-glucoside depends on the pH. In a typical experiments, different amounts of 0.001 M standard solutions of HCl and NaOH were added in an aqueous solutions of cyanidin 3,5-di-*O*-glucoside separately. The observed results are summarized in the following Scheme 3.

In aqueous solution, cyanidin participates in the acid–base equilibrium and different color persist in solution [40]. Under our experimental conditions (Table 1), red color species of cyanidin is the major existing species, which reacts with $AuCl_4^-$. A possible mechanism is

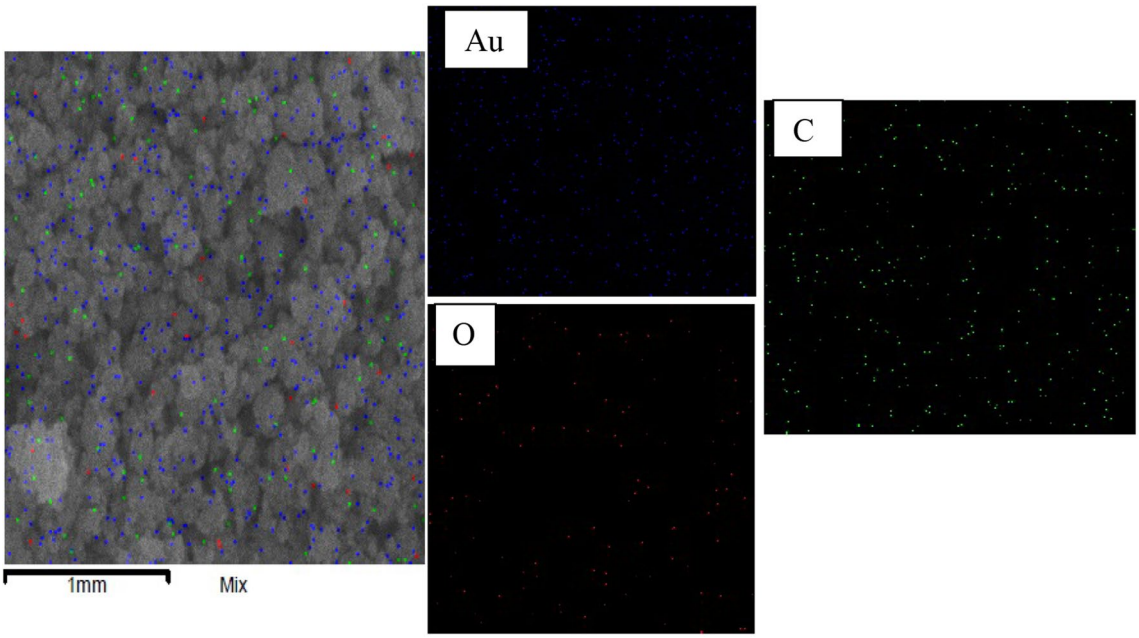

Fig. 3 Elemental mapping of anthocyanin-capped gold NPs

Table 1 Effects of [$HAuCl_4$], [cyanidin 3,5-di-*O*-glucoside anthocyanin], [CTAB] and pH on the stability, color, and SRP peak position of gold NPs

10^5[$HAuCl_4$] (mol/L)	10^5[Anthocyanin] (mol/L)	10^4[CTAB] (mol/L)	pH	Stability, color, SRP position
0.0	3.5	0.0	3.2	Red, stable[a]
0.0	3.5	0.0	4.5	Red, stable[a]
0.0	3.5	0.0	6.0	Pale Red, stable[a]
0.0	3.5	0.0	7.5	Violet, stable[b]
0.0	3.5	0.0	9.5	Violet, stable[b]
0.0	3.5	0.0	11.2	Blue, stable[b]
25	0.0	10.0	5.2	CTA-Au complex, stable
25	3.5	0.0	6.3	Yellow turbidity
25	3.5	10.0	5.1	Pale yellow, stable, 552 nm
30	3.5	10.0	5.2	Pale yellow, stable, 555 nm
40	3.5	10.0	5.2	Yellow, stable, 562 nm
50	3.5	10.0	5.0	Purple. stable, 548 nm
60	3.5	10.0	5.2	Purple, stable, 544 nm
25	1.5	10.0	5.1	Pale yellow, stable, 552 nm
25	2.5	10.0	5.0	Pale yellow, stable, 552 nm
25	3.0	10.0	5.1	Pale yellow, stable, 552 nm
25	3.5	2.0	5.6	Pale yellow, unstable, turbid
25	3.5	6.0	5.1	Pale yellow, stable, 552 nm
25	3.5	12.0	5.1	Pale yellow, stable, 552 nm

[a]pH was adjusted by using standard HCl and NaOH of cyanidin 3,5-di-*O*-glucoside solution

[b]stability was reported to the formation of perfect transparent gold sols

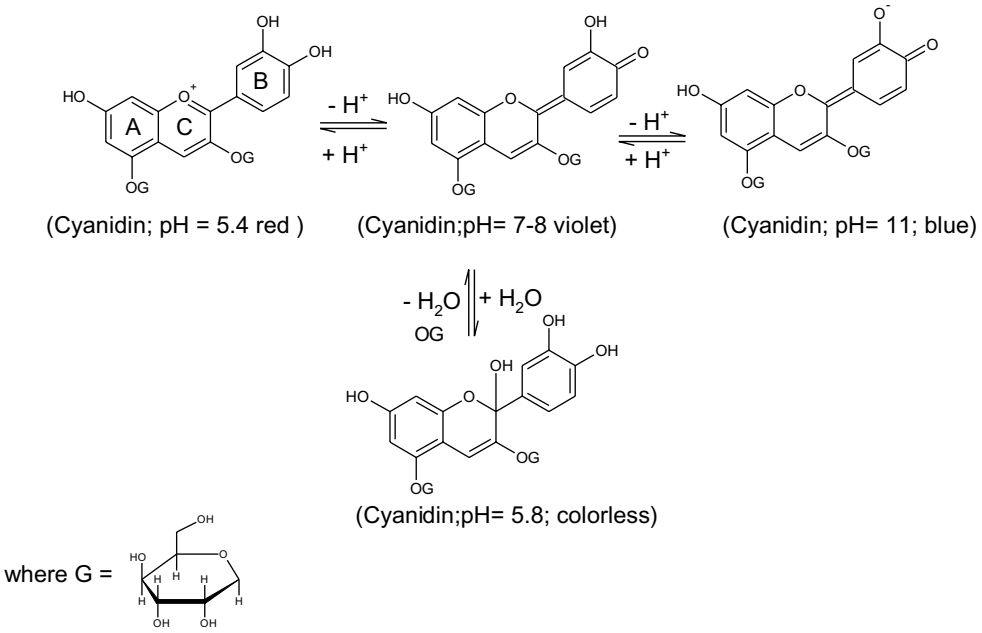

Scheme 3 Effect of pH on the color species of cyanidin 3,5-di-*O*-glucoside

Scheme 4 Reduction of gold salt by reactive species of anthocyanin

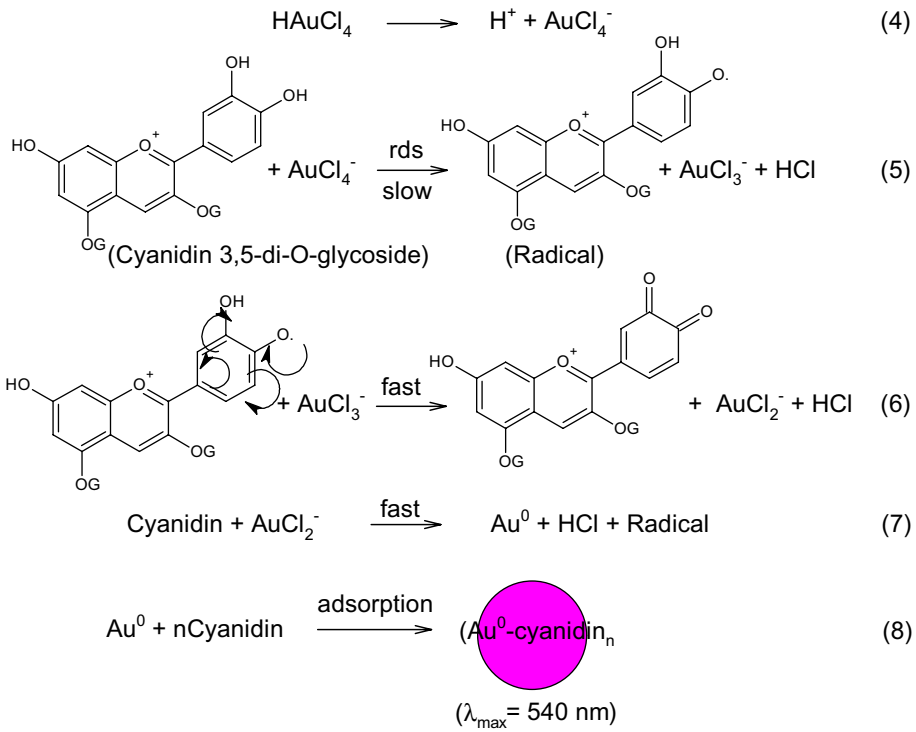

proposed for the reduction of gold salt, $HAuCl_4$, by active anthocyanin, cyanidin 3,5-di-*O*-glucoside of RRF extract (Scheme 4).

In Scheme 4, Eq. (4) represents the ionization of gold salt. Equation (5) is a one-step redox reaction between $AuCl_4^-$ and cyanidin 3,5-di-*O*-glucoside (rate-determining step). The $AuCl_3^-$ and a corresponding radical were formed. The resulting cyanidin radical was converted into the stable product, i.e., corresponding quinone (Eq. 6). In excess of cyanidin, $AuCl_2^-$ undergoes one-electron transfer mechanism to give radical and metallic gold (Eq. 7). Finally, cyanidin adsorbs on to the surface of gold metal and yields stable gold nanoparticles (Scheme 5).

3.4 Effect of gold salt on the SRP of nanoparticles

The absorption spectra of cyanidin 3,5-di-*O*-glucoside are depicted in Fig. 4a for two different cyanidin 3,5-di-*O*-glucoside concentrations (inset-*O*ptical images of cyanidin 3,5-di-*O*-glucoside). Aqueous solution shows two absorptions around at 312 and 522 nm, which might be due to the presence of 85% cyanidin 3,5-di-*O*-glucoside anthocyanin in the as-prepared extract [41]. The molar concentration of cyanidin 3,5-di-*O*-glucoside-based anthocyanin was calculated by using Lambert–Beer's law [42] (Eq. 9).

$$Absorbance = \varepsilon c l \tag{9}$$

where all symbols have their usual significance (ε = molar absorptivity, c = concentration, and l = path length). The ε = 30,247 L/mol cm was used for the calculation of molar concentration at 25 °C [43]. Upon addition of cyanidin 3,5-di-*O*-glucoside aqueous solution into the $HAuCl_4$ solution in the presence of CTAB, a characteristic peak of pure gold salt (attributed to the ligand–metal transitions; $p_\sigma \rightarrow 5dx^2 - y^2$) is not observed at ca. 288 nm, indicating that the $HAuCl_4$ converted into Au^0 (Fig. 4b). The intensity of cyanidin 3,5-di-*O*-glucoside anthocyanin peak is dramatically affected as the growth of AuNPs proceeds. The resulting purple gold sol shows a SRP band at 545 nm. The position and intensity SRP band depend on the concentration of gold salt (Table 1). Our spectra showed only one transverse peak ca. 545–580 nm. The band position strongly depends on the [$HAuCl_4$], indicating that the resulted AuNPs should be isotropic. It is well known that appearance of a single SRP band in the visible region and their shifting (either blue or red) would be due to their collective absorbance arising from surface resonance plasmon of nanospheres [44, 45]. Effects of different $HAuCl_4$ concentration are depicted graphically in Fig. 4b as a absorbance–wavelength reaction profiles. The blue- and red-shifts depend on the reaction condition. A red-shift was observed at higher [$HAuCl_4$] from 25.0×10^{-5} to 30.0×10^{-5} mol/L, probably due to the formation of bigger size of gold NPs.

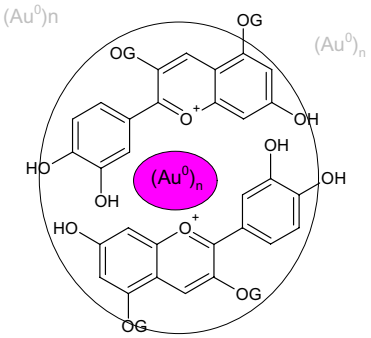

Scheme 5 Stabilization of gold NPs by cyanidin 3,5-di-*O*-glucoside

UV–Vis diffuse reflectance spectra of AuNPs are presented in Fig. 5a. The SPR band appeared at 545 nm, which might be due to the excitation of interband 6sp electrons of gold [46, 47]. The 5d-6sp optical band gap energy of AuNPs was determined from the UV–Vis diffuse reflectance spectrum in the UV-region by using Tauc's relation (Eq. 10).

$$(\alpha h\upsilon)^2 = A(h\upsilon - E_g) \tag{10}$$

where A = transition probability, h = Planck constant, υ frequency, and E_g = optical bans gap energy. Equation (10) can be written as Eq. (11) for unit transition probability.

$$(\alpha h\upsilon)^2 = h\upsilon - E_g \tag{11}$$

The E_g was calculated from the plot of $(\alpha h\upsilon)^2$ versus energy of light; hυ (Fig. 5b) by extrapolating a straight line to the $(\alpha h\upsilon)^2 = 0$ axis and found to be 3.54 eV. Our calculated E_g value is in good agreement to the band gap energy (3.52 eV) determined by Tian et al. for the AuNPs [48].

3.5 Antiradical and antimicrobial activities

The polyhydroxy phenols of natural pigments were responsible for the antioxidant and antimicrobial properties. The red rose petals were widely used for medicinal, cosmetic, and food industries. Therefore, it was to determine the total phenolic content present in the RRF extract. The UV–Vis technique was used for the estimation of phenolic content and was found to be 102.34 mg/g of dry plant material. Antiradical and antimicrobial activities of isolated anthocyanin and as-prepared anthocyanin capped gold nanoparticles were determined against DPPH radical and two human pathogens by using UV–Vis spectroscopy. For DPPH radical, IC_{50} value was evaluated from the plot of inhibition percentage versus cyanidin concentration. The IC_{50} = 52.2 µg/ml $DPPH^{\cdot}$ was determined. Antioxidant activity of polyphenols depends on the transfer of labile H- atom to $DPPH^{\cdot}$. The dihydroxyl groups of B ring of anthocyanin were responsible for the antiradical activity with radical (Scheme 6).

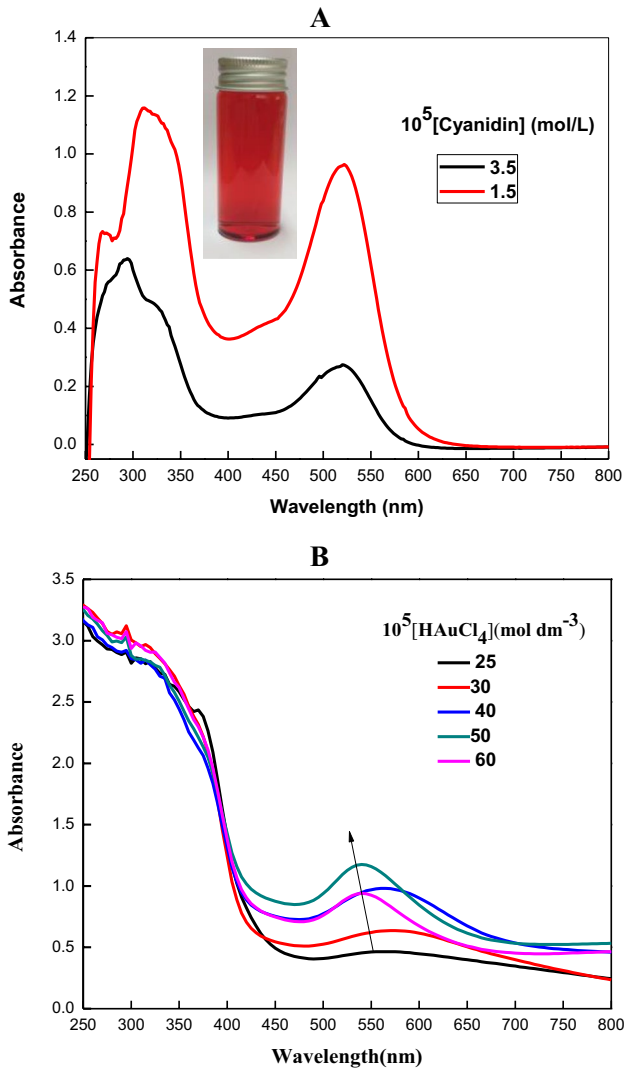

Fig. 4 UV–Vis spectra of cyanidin 3,5-di-*O*-glucoside (**a**) and effects of $HAuCl_4$ concentration on the SRP intensity and peak position of Au NPs (**b**). *Reaction conditions*: $[CTAB] = 10.0 \times 10^{-4}$ mol/L, Time = 1 h

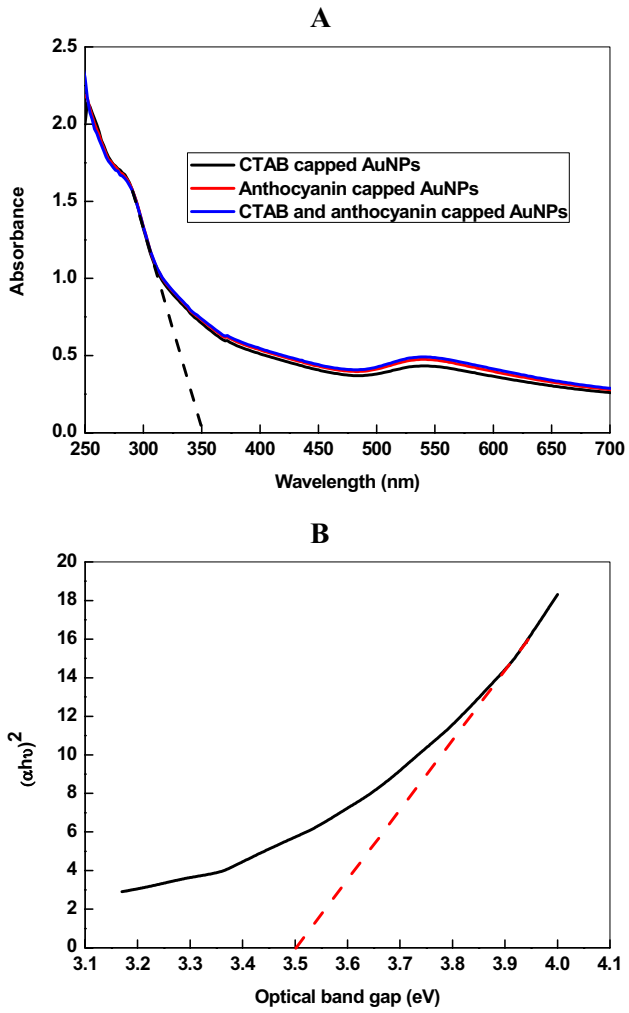

Fig. 5 UV–Vis diffuse reflectance spectra of AuNPs under different conditions (**a**) and derived Tauc plot of anthocyanin capped AuNPs (**b**)

The cyanidin 3,5-di-*O*-glucoside and gold NPs were screened for their antimicrobial properties against human pathogens by using disk-diffusion method [49]. The obtained data, photograph of diffusion zone, is given in Fig. 6. The area of inhibition zone increases with an increase in the cyanidin 3,5-di-*O*-glucoside concentration. The inhibition percentage was calculated by using following equation:

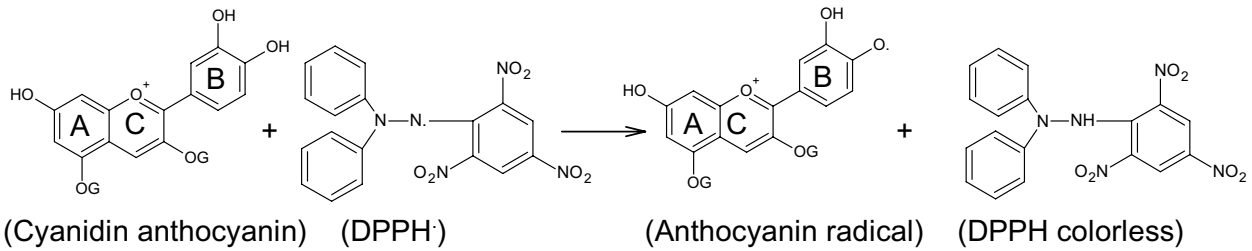

Scheme 6 Antioxidant activity of cyanidin 3,5-di-*O*-glucoside anthocyanin

$$\%\ inhibition = \frac{100 \times (cyanidin\ inhibition\ area - solvent\ inhibition\ area)}{gentamicin\ inhibition\ area - solvent\ inhibition\ area} \quad (12)$$

The inhibition area of each experiment was calculated with Eq. (13).

$$Area = \pi r^2 \quad (13)$$

where r = radius of the zone of the inhibition and $\pi = 3.14$. The plots of % inhibition against the concentrations of cyanidin 3,5-di-*O*-glucoside anthocyanin and gold NPs are depicted graphically in Fig. 7a and b, respectively. Inspection of these results suggests that the inhibition % significantly with concentrations of cyanidin 3,5-di-*O*-glucoside and gold NPs. These results can be rationalized due to the antioxidant activity of free cyanidin 3,5-di-*O*-glucoside as well as on the surface of gold NPs. He and Giusti reviewed the antimicrobial properties and other medicinal applications of anthocyanin [50]. Our results showed that cyanidin 3,5-di-*O*-glucoside and gold NPs were active against all the microorganisms used (Table 2). Metal and metal NPs have strong tendency to coordinates with protein and amino acids through electrostatically under physiological pH. The NPs

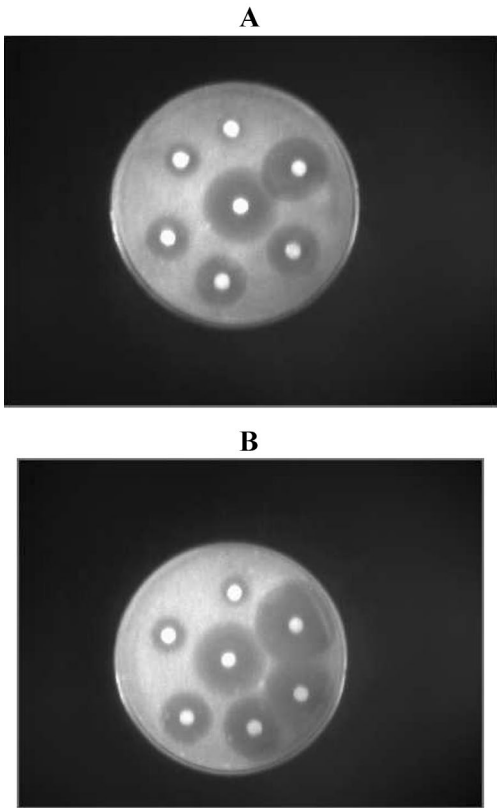

Fig. 6 Disk diffusion assay of gold NPs against *S. aureus* (**a**) and *E. coil* (**b**)

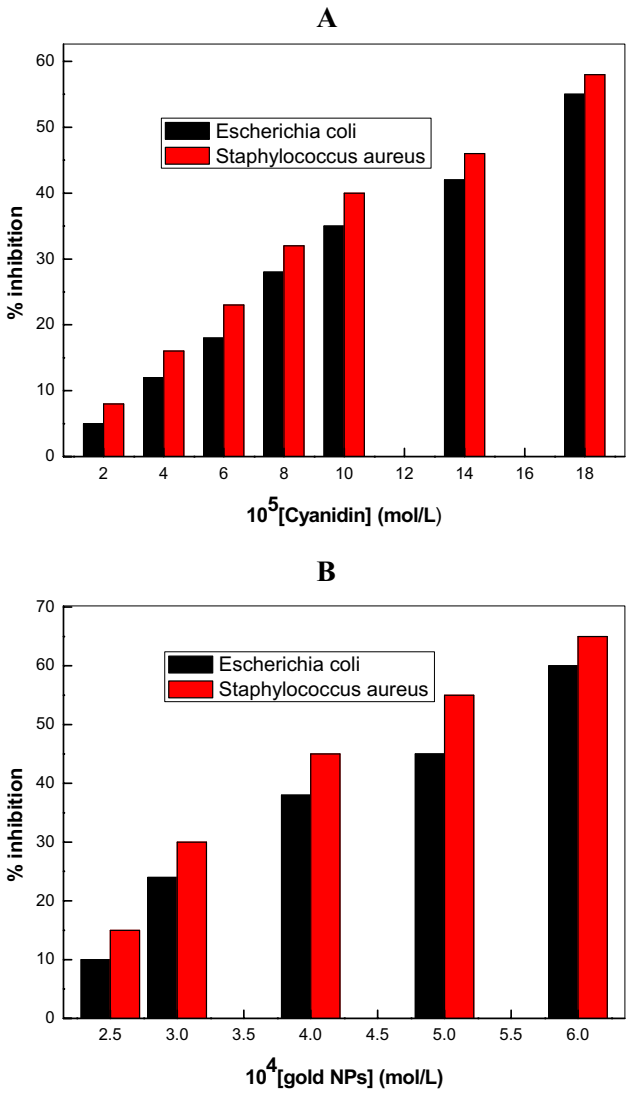

Fig. 7 **a** Effects of cyanidin 3,5-di-*O*-glucoside and (**b**) anthocyanin-capped gold nanoparticles on the antibacterial activity against human pathogens

incorporate into the cell wall of human pathogens due to synergistic coordination with the pH sensitive functional groups, altered the membrane stability and disturbed the normal structure of bacteria. They also damaged the structure of DNA and inhibit planktonic growth. As a result, the NPs exhibit antibacterial and antifungal activities. Amino acids have three potential ($-NH_2$, –COOH and –SH) coordination sites. The gold NPs coordinated with protein of bacteria cell membrane through cysteine–SH group, and released gold ions into the cell wall after oxidation of cysteine [51–54].

3.6 Eosin yellow decomposition

In order to determine the catalytic activity of AuNPs, UV–Vis spectra of eosin yellow and $NaBH_4$ (source of hydrogen) were

Table 2 Antiradical and antimicrobial activities of cyanidin 3,5-di-*O*-glucoside anthocyanin and gold NPs

Sample	Antiradical activity (g/µml)	Inhibition zone (mm)		MIC (µg/ml)	
		S. aureus	*E. coli*	*S. aureus*	*E. coli*
Cyanidin	52.2 ± 1.5	14	10	30	25
Gold NPs	60.7 ± 2.5	20	17	40	30
Gentamicine		23	21	25	22
	Antifungus activity	Inhibition zone (mm)		MIC (µg/ml)	
	C. albicans	*C. parapsilosis*	*C. albicans*	*C. parapsilosis*	
Cyanidin	12	16	40	55	
Gold NPs	16	20	47	54	
Fluconazole	10	12	25	22	

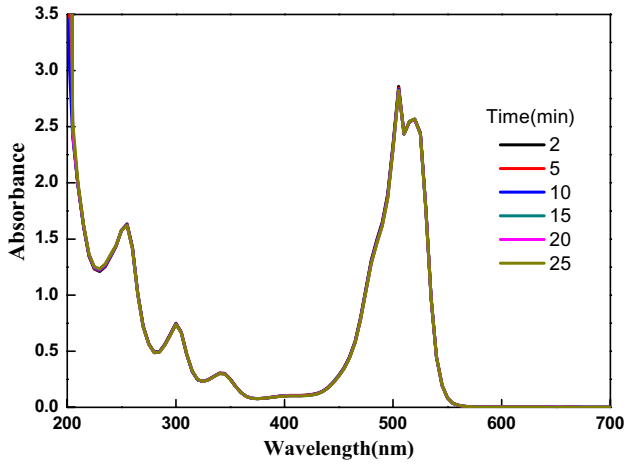

Fig. 8 Effect of $NaBH_4$ on the degradation of eosin yellowish. *Reaction conditions*: [Eosin yellowish] = 2.0×10^{-5} mol/dm^3 and [$NaBH_4$] = 3.4×10^{-3} mol dm^3

recorded as a function of time. Figure 8 shows that the aqueous solution of eosin yellow sodium salt exhibits 3 week peaks and one most intense peak at 254, 301, 342, and 517 nm, respectively, for benzene ring, carbonyl group in the benzene ring, –COOH group, and polycyclic conjugated aromatic chromosphere. Therefore, the dye degradation was monitored at 517 nm for oxidative and photocatalytic decomposition. Interestingly, $NaBH_4$ shows no effect on the spectrum of dye, which remains same with respect to peak intensity and peak position (λ_{max}). Thus, eosin yellow is stable with $NaBH_4$ solution for ca. 30 min (Fig. 8). In the next experiment, AuNPs and $NaBH_4$ added into dye solution, and decolorization was recorded at different time intervals. Surprisingly, peak intensity decreased very fast at 517 nm (Fig. 9), which might be due to the combined effect of AuNPs and $NaBH_4$. The apparent first-order rate constant (k_{app}) and degradation % were calculated by using Eqs. (14) and (15).

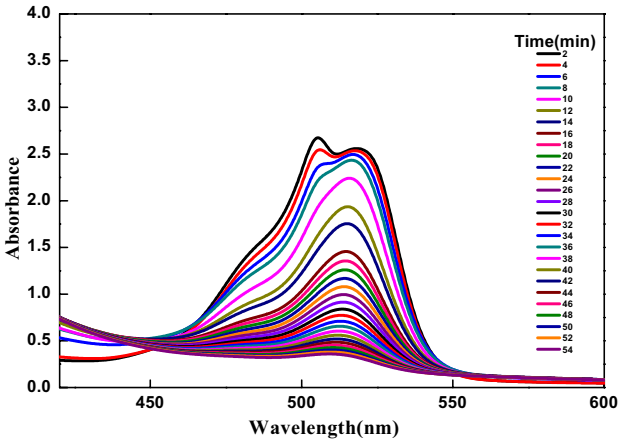

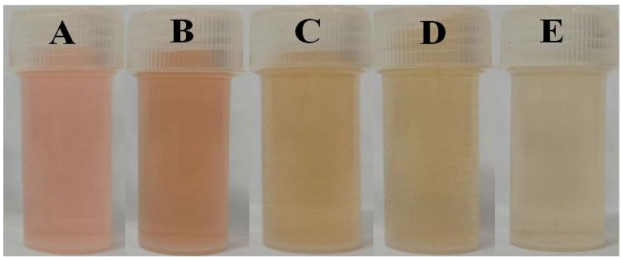

Fig. 9 Degradation time-resolved UV–Vis spectra and optical images of eosin yellow degradation by gold NPs in the presence of $NaBH_4$. *Reaction conditions*: [Eosin yellow] = 2.0×10^{-5} mol dm^{-3}, [gold NPs] = (3.4×10^{-4} mol/L), [$NaBH_4$] = 3.4×10^{-3} mol dm^3 (Color figure online)

$$k_{app} = \frac{1}{t} \ln \left(\frac{A_0}{A_t} \right) \tag{14}$$

$$Degradation\ ratio\ \% = \left(1 - \frac{A_t}{A_0} \right) \times 100 \tag{15}$$

Kinetic experiments were carried out at different [$NaBH_4$] ranging from 3.4×10^{-3} to 10.0×10^{-3} mol/L with a fixed [eosin] (2.0×10^{-4} mol/L), [AuNPs] (3.4×10^{-4} mol/L) and temperature (303 K). The k_{ppp} values increases with [$NaBH_4$] (Table 3). Figure 10a shows that the dye decolorization follows excellent first-order kinetics. Inspection of Fig. 10a and b indicates that the rate of degradation strongly depends on the $NaBH_4$ at constant AuNPs. At higher $NaBH_4$, eosin yellow became colorless completely with in ca. 15 min. Table 3 shows that the [eosin], [AuNPs], and sun light irradiation have significant effect on the decolorization of dye. In order to determine the activation energy, enthalpy of activation, and entropy of activation, the effect of temperature (from 303 to 323 K) was studied at fixed concentration of dye (2.0×10^{-5} mol/L), $NaBH_4$ (3.4×10^{-3} mol/L), and catalyst (3.4×10^{-4} mol/L). The k_{app} values increases with temperature (Table 4). Arrhenius (Eq. 16; Fig. 11a) and Eyring (Eq. 17; Fig. 11b) equations were used for the calculation of activation parameters (energy of activation, enthalpy ($\Delta H^{\#}$) and entropy ($\Delta S^{\#}$).

$$\ln k_{app} = -\frac{E_a}{R}\left(\frac{1}{T}\right) + \ln A \tag{16}$$

$$k_{app} = \frac{\kappa_B T}{h} e^{\frac{\Delta S\#}{R}} e^{-\frac{\Delta H\#}{RT}} \tag{17}$$

The E_a was found to be 54.4 kJ/mol and 39.5 kJ/mol from the slopes of Arrhenius plots for oxidative- and photocatalytic degradation of eosin dye. Lower value of activation energy indicates that the sun light-assisted degradation is fast than that of oxidative.

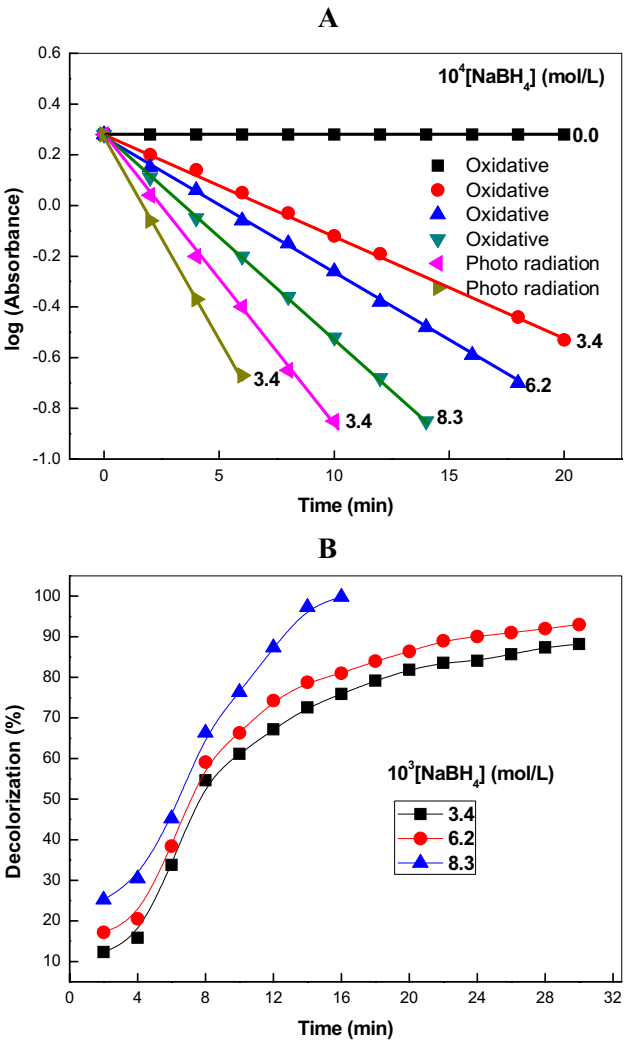

Fig. 10 Apparent first-order [log(Absorbance) versus time (**a**)] and degradation% versus time (**b**) plots for eosin yellow degradation

Table 3 Effects of [$NaBH_4$], [AuNPs], pH and sunlight on the degradation of eosin yellow at 303 K

10^3[$NaBH_4$] (mol/L)	10^4[AuNPs] (mol/L)	10^5[Eosin yellow] (mol/L)	pH	10^3 k_{app} (s^{-1})	Sunlight radiation[a] 10^3 k_{app}/s
0.0	3.4	2.0	6.7	0.0	0.2
3.4	0.0	2.0	8.3	0.0	0.0
3.4	3.4	2.0	8.3	1.5	5.5
6.2	3.4	2.0	8.5	1.9	7.3
8.3	3.4	2.0	8.6	3.0	8.6
10.0	3.4	2.0	8.6	3.4	10.1
3.4	3.8	2.0	8.3	2.2	
3.4	4.2	2.0	8.3	2.9	
3.4	3.4	1.2	8.3	0.8	
3.4	3.4	3.4	8.3	2.8	
3.4	3.4	3.4	8.3	3.5	

[a]Sun light irradiation for 20 min

Table 4 Values of rate constant and activation parameters for the degradation of eosin yellow

Temperature (K)	$10^3\ k_{app}$ (s^{-1})	E_a (kJ/mol)	$\Delta H^{\#}$ (kJ/mol)	$\Delta S^{\#}$ (kJ/mol)	Scavenger[a]	$10^3\ k_{app}$ (s^{-1})
303	1.5(5.5)[a]	54(39)	56(40)	−18(−54)	CH_3OH	0.8
313	3.0(10.2)				$KBrO_3$	0.5
323	6.1(14.3)				KI	0.2
					AO	1.2
					BQ	1.1

AO ammonium oxalate and *BQ* benzoquinone

[a]Sun light irradiation for 20 min

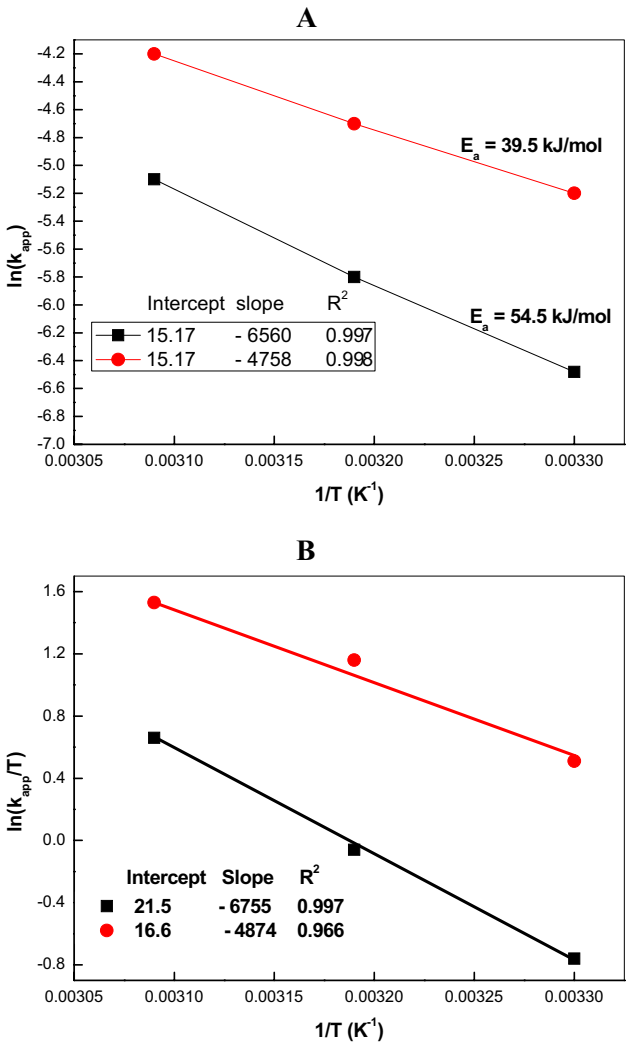

Fig. 11 Arrhenius (**a**) and Eyring (**b**) plots for the eosin yellow degradation

3.7 Mechanism of dye degradation

Eosin participates in acid–base equilibrium and various species exist in the solution (Scheme 8). The position of wavelength maxima and intensity of peak depends on the pH of the working conditions. Therefore, pH of the reaction mixture (AuNPs + eosin + $NaBH_4$) was recorded at different time intervals, which was nearly constant (pH = 8.7) during the dye degradation (Table 3). Under our experimental conditions, Y^{2-} is the major and reactive species of eosin (Scheme 7).

Figure 9 clearly shows that the both AuNPs and $NaBH_4$ would be essential for the eosin degradation. Surprisingly, no dye degradation was observed in the presence of only AuNPs and $NaBH_4$. Thus, Scheme 8 is proposed for the decolorization.

Scheme 8 represents the adsorption of dye (Y^{2-}) and BH_4^- onto the surface of AuNPs. Hydrogen transported to dye via the surface of AuNPs through electron relay effect, which leads to the formation of eosin leuco form. Our results are in agreement with the suggestions of Pal and his coworkers regarding the role of metal NPs on the decomposition of nitro compounds with $NaBH_4$ [55, 56].

To see insight into the catalytic role of sun light irradiation, the effect of some radical scavengers (methanol, benzoquinone, potassium bromate, potassium iodide, and ammonium oxalate) was studied to quench active oxygen radical species (hydroxyl ($^{\cdot}OH$, superoxide ($^{\cdot-}O{=}O$), electrons (e^-), and holes (h^+) [57]. The values of degradation rate constants decreased upon addition of these scavengers (Table 3). It is well known that molecular oxygen acts as an oxidant in the photocatalytic degradation of organic compounds due to the transfer of electrons from organic molecule to oxygen. The generated species ($^{\cdot}OH$ and $^{\cdot-}O{=}O$) due to the oxidation and reduction of water and oxygen on the surface of AuNPs via surface plasmon resonance effect (transition of 5d electrons to the 6sp band) act as catalyst [46, 48, 58]. The resulted $^{\cdot}OH$ and $^{\cdot-}O{=}O$ are responsible to the photocatalytic decomposition of eosin dye. AuNPs exhibited a SPR band at ca. 545 nm, which originates from the excitation of electrons from 5d to 6sp (Scheme 9) [46, 48, 58].

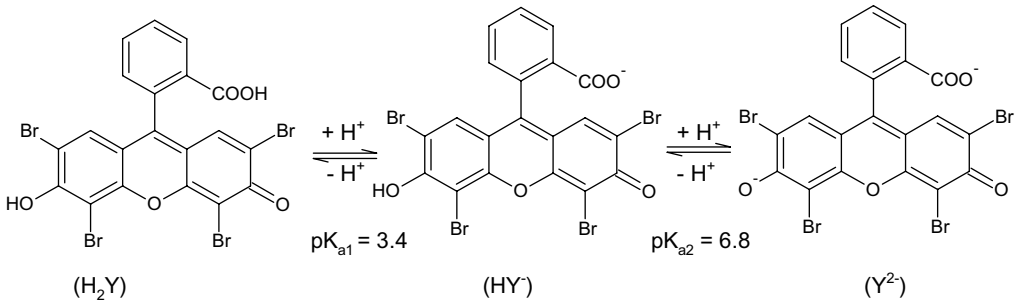

Scheme 7 Protonation of eosin dye in an aqueous solution

Scheme 8 Role of AuNPs on the decolorization of eosin

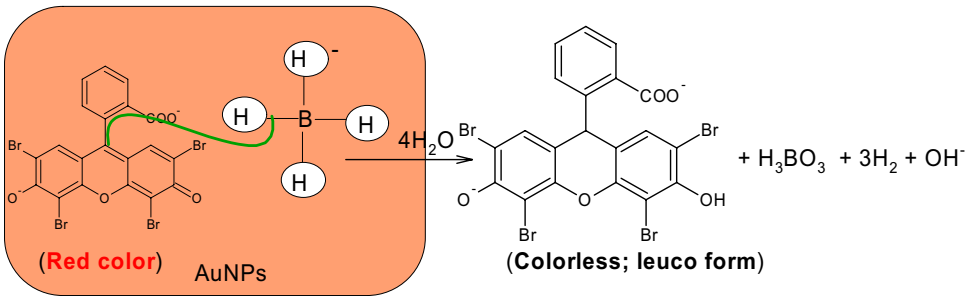

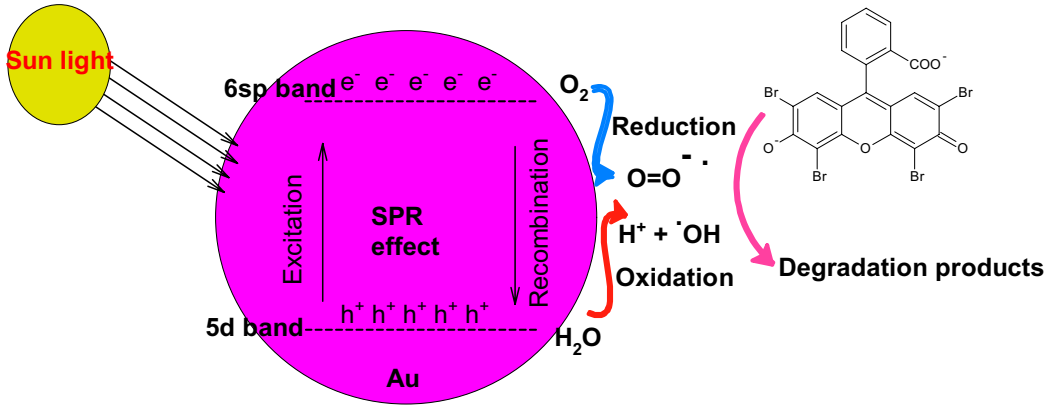

Scheme 9 Effect of sun light on the decomposition of eosin

4 Conclusion

We demonstrated a facile extraction of cyanidin 3,5-di-*O*-glucoside from the red orange rose petals at room temperature. The extracted cyanidin 3,5-di-*O*-glucoside was used for the preparation of gold NPs with and without cationic surfactant, CTAB. UV–Vis and TEM data indicate that the $HAuCl_4$ forms a pale yellow colored complex with ionized CTAB having nanoflower like morphology. The controlled morphology of the gold NPs is presented by adjusting the concentration ratio of $HAuCl_4$, CTAB to cyanidin 3,5-di-*O*-glucoside. The cyanidin 3,5-di-*O*-glucoside and cyanidin-capped gold NPs exhibited excellent inhibitory effect against *S. aureus*, *E. coil,* and candida fungus, which might be due to the synergistic effect of gold NPs and the presence of anthocyanin on the surface of NPs. The eosin was used as a model dye to determine the oxidative and photocatalytic activities of AuNPs. The k_{app} value (3.4×10^{-3} s^{-1}) obtained for the decolorization of eosin with $NaBH_4$ was ca. three time lower than that of sun light irradiation $k_{app} = 10.1 \times 10^{-3}$ s^{-1}. Low activation energy (39 kJ/mol) and moderate activation entropy (-54 JK^{-1} mol^{-1}) indicate the formation of highly disorder system on the surface of nanocatalyst due to the generation of reactive oxygen radicals.

Acknowledgements This project was funded by the Deanship of Scientific Research (DSR) at King Abdulaziz University, Jeddah, under Grant No. (D-178-274-1439). The authors, therefore, acknowledge with thanks DSR for technical and financial support.

Compliance with ethical standards

Conflict of interest Authors declare that there is no conflict of interest.

References

1. M.-C. Daniel, D. Astruc, Gold nanoparticles: assembly, supramolecular chemistry, quantum-size-related properties, and applications toward biology, catalysis, and nanotechnology. Chem. Rev. **104**, 293–346 (2004)
2. A. Henglein, D. Meisel, Radiolytic control of the size of colloidal gold nanoparticles. Langmuir **14**, 7392–7394 (1998)
3. K. Esumi, K. Matsuhisa, K. Torigoe, Preparation of rodlike gold particles by UV irradiation using cationic micelles as a template. Langmuir **11**, 3285–3287 (1995)
4. D.V. Goia, E. Matijevic, Tailoring the particle size of monodispersed colloidal gold. Coll. Surf. A **146**, 139–152 (1999)
5. K. Jadhav, H.R. Rajeshwari, S. Deshpande, S. Jagwani, D. Dhamecha, S. Jalalpure, K. Subburayan, D. Baheti, Phytosynthesis of gold nanoparticles: characterization, biocompatibility, and evaluation of its osteoinductive potential for application in implant dentistry. Mater. Sci. Eng. C **93**, 664–670 (2018)
6. M.S. Bakshi, F. Possmayer, N.O. Petersen, Role of different phospholipids in the synthesis of pearl-necklace-type gold-silver bimetallic nanoparticles as bioconjugate materials. J. Phys. Chem. C **111**, 14113–14124 (2007)
7. M.S. Bakshi, H. Kaur, T.S. Banipal, N. Singh, G. Kaur, Biomineralization of gold nanoparticles by lysozyme and cytochrome c and their applications in protein film formation. Langmuir **26**, 13535–13544 (2010)
8. M.S. Bakshi, Colloidal micelles of block copolymers as nanoreactors, templates for gold nanoparticles, and vehicles for biomedical applications. Adv. Coll. Interface Sci. **213**, 1–20 (2014)
9. B. Nikoobakht, M.A. El-Sayed, Preparation and growth mechanism of gold nanorods (NRs) using seed-mediated growth method. Chem. Mater. **15**, 1957–1962 (2003)
10. S. Khademi, S. Sarkar, A. Shakeri-Zadeh, N. Attaran, S. Kharrazi, M. RezaAy, H. Ghadiri, Folic acid-cysteamine modified gold nanoparticle as a nanoprobe for targeted computed tomography imaging of cancer cells. Mater. Sci. Eng. C **89**, 182–193 (2018)
11. Z. Shervani, Y. Yamamoto, Carbohydrate-directed synthesis of silver and gold nanoparticles: effect of the structure of carbohydrates and reducing agents on the size and morphology of the composites. Carbohydr. Res. **346**, 651–694 (2011)
12. P.C. Pandey, G. Pandey, A. Walcarius, 3-Aminopropyltrimethoxysilane mediated solvent induced synthesis of gold nanoparticles for biomedical applications. Mater. Sci. Eng. C **79**, 45–54 (2017)
13. Z. Khan, T. Singh, J.I. Hussain, A.A. Hashmi, Au(III)-CTAB reduction by ascorbic acid: preparation and characterization of gold nanoparticles. Coll. Surf. B **104**, 11–17 (2013)
14. M.N. Khan, T.A. Khan, S.A. Al-Thabaiti, Z. Khan, Spectrophotometric evidence to the formation of $AuCl_4$-CTA complex and synthesis of gold nano-flowers with tailored surface textures. Spectrochim. Acta A **149**, 889 (2015)
15. L. Longenberger, G. Mills, Formation of metal particles in aqueous solutions by reactions of metal complexes with polymers. J. Phys. Chem. **99**, 475–478 (1995)
16. X. Liu, M. Atwater, J. Wang, Q. Huo, Extinction coefficient of gold nanoparticles with different sizes and different capping ligands. Coll. Surf. B **58**, 3–7 (2007)
17. P.-L. Kuo, C.-C. Chen, M.-W. Jao, Effects of polymer micelles of alkylated polyethylenimines on generation of gold nanoparticles. J. Phys. Chem. B **109**, 9445–9450 (2005)
18. M.H. Mashhadizadeh, R.P. Talemi, Synergistic effect of magnetite and gold nanoparticles onto the response of a label-free impedimetric hepatitis B virus DNA biosensor. Mater. Sci. Eng. C **59**, 773–781 (2016)
19. B. Kumar, K. Smita, L. Cumbal, J. Camacho, E. Hernández-Gallegos, M. G. Chavez-Lopez, M. Grijalva, K. Andrade, One pot phytosynthesis of gold nanoparticles using Genipa americana fruit extract and its biological applications. Mater. Sci. Eng. C **62**, 725–731 (2016)
20. S.P. Dubey, M. Lahtinen, M. Sillanpaa, Tansy fruit mediated greener synthesis of silver and gold nanoparticles. Process Biochem. **45**, 1065–1071 (2010)
21. R. Geetha, T. Ashokkumar, S. Tamilselvan, K. Govindaraju, M. Sadiq, G. Singaravelu, Green synthesis of gold nanoparticles and their anticancer activity. Cancer Nano **4**, 91–98 (2013)
22. C.H. Eugster, E. Marki-Fischer, The chemistry of rose pigments. Angew. Chem. Int. Ed. Engl. **30**, 654–672 (1991)
23. M.H. Eikani, F. Golmohammad, S. Rowshanzamir, M. Mirza, Recovery of water-soluble constituents of rose oil using simultaneous distillation-extraction. Flavour Fragr. J. **20**, 555–558 (2005)
24. R. Nowak, M. Olech, Ł. Pecio, W. Oleszek, R. Los, A. Malm, J. Rzymowska, Cytotoxic, antioxidant, antimicrobial properties and chemical composition of rose petals. J. Sci. Food Agric. **94**, 560–567 (2014)
25. M.S. Bakshi, Nanoshape control tendency of phospholipids and proteins: Protein-nanoparticle composites, seeding, self-aggregation, and their applications in bionanotechnology and nanotoxicology. J. Phys. Chem. C **115**, 13947–13960 (2011)
26. S.S. Shankar, A. Rai, A. Ahmad, M. Sastry, Rapid synthesis of Au, Ag, and bimetallic Au core-Ag shell nanoparticles using Neem (*Azadirachta indica*) leaf broth. J. Coll. Interface Sci. **275**, 496–502 (2004)
27. N.R. Jana, L. Gearheart, C.J. Murphy, Seed-mediated growth approach for shape-controlled synthesis of spheroidal and rodlike gold nanoparticles using a surfactant template. Adv. Mater. **13**, 1386–1389 (2001)
28. V.L. Singleton, J.A. Jr Rossi, Colorimetry of total phenolics with phosphomolybdic-phosphotungstic acid reagents. Am. J. Enol. Vitic. **16**, 144–158 (1965)
29. J.B. Harbornem, Spectral methods of characterizing anthocyanins. Biochem. J. **70**, 22–28 (1958)
30. T. Fulehi, F.J. Francis, Quantitative methods for anthocyanins. 1. Extraction and determination of total Anthocyanin in cranberries. J. Food Sci. **33**, 72–77 (1968)
31. Z. Zaheer, Eco-friendly walnut shell powder based facile fabrication of Ag-nanodisks, and their interaction with bovine serum albumin. J. Photochem. Photobiol. B **193**, 8–17 (2019)
32. J. Xiao, L. Qi, Surfactant-assisted, shape-controlled synthesis of gold nanocrystals. Nanoscale **3**, 1383–1396 (2011)
33. L. Li, Z. Wang, T. Huang, J. Xie, L. Qi, Porous gold nano belts templated by metal-surfactant complex nanobelts. Langmuir **26**, 12330–12335 (2010)
34. F. Bodker, S. Morup, S. Linderoth, Surface effects in metallic iron nanoparticles. Phys. Rev. Lett. **72**, 282–285 (1994)
35. M. Liu, P. Guyot-Sionnest, Mechanism of silver(I)-assisted growth of gold nanorods and bipyramids. J. Phys. Chem. B **109**, 22192–22200 (2005)
36. T.K. Sau, C.J. Murphy, Room temperature, high-yield synthesis of multiple shapes of gold nanoparticles in aqueous solution. J. Am. Chem. Soc. **126**, 8648–8649 (2004)

37. J.H. Lee, H.-J. Lee, M.-G. Choung, Anthocyanin compositions and biological activities from the red petals of Korean edible rose (*Rosa hybrida* cv *Noblered*). Food Chem. **129**, 272–278 (2011)
38. M. Noruzi, D. Zare, K. Khoshnevisan, D. Davoodi, Rapid green synthesis of gold nanoparticles using rosa hybrida petal extract at room temperature. Spectrochemica. Acta A **79**, 1461–1465 (2011)
39. H.E. Khoo, A. Azlan, S.T. Tang, S.M. Lim, Anthocyanidins and anthocyanins: colored pigments as food, pharmaceutical ingredients, and the potential health benefits. Food Nutr. Res. **61**, 1361779 (2017)
40. A. Castaneda-Ovando, M.L. Pacheco-Hernandez, M.E. Paez-Hernandez, J.A. Rodriguez, C.A. Galan-Vidal, Chemical studies of anthocyanins: a review. Food Chem. **113**, 859–871 (2009)
41. R.L. Scalzo, A. Genna, F. Branca, M. Chedin, H. Chassaigne, Anthocyanin composition of cauliflower (*Brassica oleracea* L. var. botrytis) and cabbage (*B. oleracea* L. var. capitata) and its stability in relation to thermal treatments. Food Chem. **107**, 136–144 (2008)
42. Y. Cai, M. Sun, H. Wu, R. Huang, H. Corke, Characterization and quantification of betacyanin pigments from diverse amaranthus species. J. Agric. Food Chem. **46**, 2063–2070 (1998)
43. N. Ahmadiani, R.J. Robbins, T.M. Collins, M.M. Giusti, Molar absorptivity (ε) and spectral characteristics of cyanidin-based anthocyanins from red cabbage. Food Chem. **197**, 900–906 (2016)
44. A. Mahal, P. Khullar, H. Kumar, G. Kaur, N. Singh, M. Jelokhani-Niaraki, M.S. Bakshi, Green Chemistry of zein protein toward the synthesis of bioconjugated nanoparticles: understanding unfolding, fusogenic behavior, and hemolysis. ACS Sustain. Chem. Eng. **1**, 627–639 (2013)
45. B. Rodriguez-Gonzalez, P. Mulvaney, L.M. Liz-Marzan, An electrochemical model for gold colloid formation via citrate reduction. Z. Phys. Chem. **221**, 415–426 (2007)
46. S. Mondal, M.E. De Anda Reyes, U. Pal, Plasmon induced enhanced photocatalytic activity of gold loaded hydroxyapatite nanoparticles for methylene blue degradation under visible light. RSC Adv. **7**, 8633–8645 (2017)
47. H. Zhu, X. Chen, Z. Zheng, X. Ke, E. Jaatinen, J. Zhao, C. Guo, T. Xie, D. Wang, Mechanism of supported gold nanoparticles as photocatalysts under ultraviolet and visible light irradiation. Chem. Commun. **48**, 7524–7526 (2009)
48. B. Tian, Q. Lei, B. Tian, W. Zhang, Y. Cui, Y. Tian, UV-driven overall water splitting using unsupported gold nanoparticles as photocatalysts. Chem. Commun. **54**, 1845–1848 (2018)
49. R. Nowak, M. Olech, L. Pecio, W. Oleszek, R. Los, A. Malmc, J. Rzymowska, Cytotoxic, antioxidant, antimicrobial properties and chemical composition of rose petals. J. Sci. Food Agric. **94**, 560–567 (2014)
50. J.A. He, M.M. Giusti, Anthocyanins: Natural colorants with health promoting properties. Annu. Rev. Food Sci. Technolo. **1**, 163–186 (2010)
51. P. Natarajan, P. Sukthankar, J. Changstrom, C.S. Holland, S. Barry, W.B. Hunter, C.M. Sorensen, J.M. Tomich, Synthesis and characterization of multifunctional branched amphiphilic peptide bilayer conjugated gold nanoparticles. ACS Omega **3**, 11071–11083 (2018)
52. I. Sondi, B. Salopek-Sondi, Silver nanoparticles as antimicrobial agent: a case study on *E. coli* as a model for gram-negative bacteria. J. Coll. Interface Sci. **275**, 177–182 (2004)
53. Rahisuddin, S.A. Al-Thabaiti, Z. Khan, N. Manzoor, Biosynthesis of silver nanoparticles and its antibacterial and antifungal activities towards gram-positive, gram-negative bacterial strains and different species of candida fungus. Bioprocess Biosyst. Eng. **38**, 1773–1781 (2015)
54. A.I. Lopez-Lorente, S. Cardenas, Z.I. Gonzalez-Sanchez, Effect of synthesis, purification and growth determination methods on the antibacterial and antifungal activity of gold nanoparticles. Mater. Sci. Eng. C **103**, 109805 (2019)
55. T. Pal, S. De, N.R. Jana, N. Pradhan, R. Mandal, A. Pal, A.E. Beezer, J.C. Mitchel, Organized media as redox catalysts. Langmuir **14**, 4724–4730 (1998)
56. N. Pradhan, A. Pal, T. Pal, Silver nanoparticle catalyzed reduction of aromatic nitro compounds. Coll. Surf. A **196**, 247–257 (2002)
57. G. Li, K.H. Wong, X. Zhang, C. Hu, J.C. Yu, R.C.Y. Chan, P.K. Wong, Degradation of acid orange 7 using magnetic AgBr under visible light: The roles of oxidizing species. Chemosphere **76**, 1185–1191 (2009)
58. K. Yamada, K. Miyajima, F. Mafune, Thermionic emission of electrons from gold nanoparticles by nanosecond pulse-laser excitation of interband. J. Phys. Chem. C **111**, 11246–11251 (2007)

Publisher's Note Springer Nature remains neutral with regard to jurisdictional claims in published maps and institutional affiliations.